Supporting Information for:
Variability of bottom dissolved oxygen on the southern Senegalese shelf at intraseasonal to interannual time scales using a modelling approach

Abdoul Wahab Tall[a,b], Vincent Echevin[c], Xavier Capet[c], Eric Machu[d]

[a]*Department of Earth, Ocean and Atmospheric Sciences, University of British Columbia, 2020 – 2207 Main Mall, Vancouver, V6T 1Z4, British Columbia, Canada*
[b]*Laboratoire de Physique de l'Atmosphère et de l'Océan Siméon Fongang, Université Cheikh Anta DIOP de Dakar, Ecole Supérieure Polytechnique, , Dakar-Fann, 5085, , Senegal*
[c]*LOCEAN-IPSL, IRD/CNRS/Sorbonne Université (UPMC)/MNHN, UMR 7159, 4, place Jussieu, Paris, 75005, , France*
[d]*Université de Bretagne Occidentale, CNRS, IRD, Ifremer, Laboratoire d'Océanographie Physique et Spatiale (LOPS), IUEM, UMR 6523, Brest, 29280, , France*

Deep Sea Research Part II: Topical Studies in Oceanography "Eastern Boundary Upwelling Systems (EBUS): Past, Present and Future

Preprint submitted to Deep Sea Research Part II : EBUS *October 15, 2024*

The supporting information provides the supplementary figures and descriptions as cited in the main article.

We present the evaluation of physical and biogeochemical variables (except DO evaluation shown in section 4 of the main text) using available observations. Note that a physical simulation performed with the same dynamical model, slightly different forcings and over a different time period was previously evaluated against observations in Ndoye (2016).

1. Evaluation of the model physical variables

1.1. Thermal structure of the upwelling region

The SST displays a structure typical of upwelling systems, with relatively low temperature nearshore and higher temperatures offshore (Figs. S1a,b). In the SSUS, warm waters were found offshore and along the coast, separated by the upwelling plume, a tongue of cool waters extending southward from Hann Bay (14°40'N) where the upwelling was enhanced (Ndoye et al., 2014, 2017). The modelled surface waters south and west of the upwelling plume were slightly warmer than the observed.

Temperature cross-shore sections south of the upwelling center collected at the beginning (November 2019; Figs. S2a,d) and at the end of the upwelling season (June 2018; Figs. S1c,d) illustrate the model's ability to represent a typical upwelling vertical structure. The model thermal structure is comparable to the observations, despite the large vertical displacements of the isotherms (likely due to internal gravity waves and (sub)mesoscale structures; note that weak modelled internal waves are likely due to the absence of tidal forcing in our simulation). Model-data agreement is very good in June 2018, whereas the model bias is larger in November 2019 due to a thicker and warmer surface layer and reduced upwelling of cool waters. The surface mixed layer depth (MLD) in June 2018 is also relatively well represented in the model (~20 m; Figs. S1c,d).

As the upwelling center is located south of the Cap Vert peninsula (see Fig. 1a; Ndoye et al. (2017)), the Melax mooring is inside the upwelling plume. The near-surface (10 m depth) temperature displayed a marked seasonal cycle (Fig. S3a), with low values (~15-16°C and ~17-20°C in the observations and model, respectively) during the cold upwelling season (Feb-March 2015) and high values (up to ~28°C and ~30°C in the observations and model, respectively) during summer (July-October 2015). The model warm bias was slightly stronger during the 2015 cold season (~+3°C in 15 February-10 March) than during the 2016 cold season (~2°C between 20 February-15 April). Near-bottom temperatures (at 28 m depth, corresponding to the depth of the DO sensor located ~7-8 meters above the bottom) follow a similar seasonal cycle, the model temperatures remaining ~2-3°C higher than the observed during the cold season. Near-bottom temperature displayed large oscillations due to upwelling-favorable wind events and vertical mixing (e.g. in late May 2015, mid-September 2015, late October 2015) which were relatively well reproduced by the model. Note that model bottom temperature (at 36 m depth) was very close (~0.1°C difference) to the 28 m depth model temperature during the cold season. This indicates that the model bottom boundary layer was nearly $\sim$10 m thick during the cold season. In contrast, a difference of 1-2°C can be occasionally seen during summer, indicating near-bottom thermal stratification, underestimated in the model (Fig. S3b, Tall et al. (2021)).

1.2. Mixed layer depth (MLD)

The MLD showed a strong variability over intraseasonal to seasonal time scales (see Fig. 2d in Tall et al. (2021)). The model tends to overestimate the mixed layer during the upwelling season, occasionally reaching the bottom of the shelf (Fig. S3c). In terms of DO dynamics, this implies that the coastal sector whose bottom waters are replenished with DO through vertical mixing extends further offshore in the model than in the observations. The mixed layer was thinner (~10-20 m) and more realistically reproduced by the model during the warm season (June-November). Note that using a model parameterization (not used in the present study) including the effect of chlorophyll-shading on the thermal structure (e.g. Echevin et al. (2021)) decreased the modelled mixed layer by ~5 m, reducing bias during the upwelling season (Chabert et al., 2023).

1.3. Bottom current variability over the mid-shelf

Time series of the bottom layer currents (averaged between 30-36 m depth) at the Melax station over two distinct time periods (from mid-February to mid-June 2015, and from the end of November 2015 to April 2016) were compared to the model currents (Fig. S4). The observed currents displayed a stronger variability at synoptic ($<$10 days) time scales than the modelled. Modelled and observed zonal currents did not match up in general, except during time periods of a few weeks (end of February 2015; Mid-May-June 2015; Fig. S4a; Mid-February-end of April 2016; Fig. S4b). Isobaths being approximately oriented north-south at the mooring site, zonal velocities reflect across-shore transport which are notoriously difficult to represent (McCabe et al., 2015). Model and observed meridional (along-shore) near-bottom velocities were relatively coherent during several time periods, especially in Mid-March- April 2015; late May-June 2015 Fig. S4b); Mid-March-April 2016 (Fig. S4d). Variability at ~15-20 days was weak in the model, pointing to a possible lack of energetic coastal trapped waves in the southern boundary (~8°N) forcing. This bias may be partly attributed to the smoothing of bottom topography required by CROCO numerics (Shchepetkin and McWilliams, 2003) but we suspect that deficiencies in the remote forcing provided at the southern boundary condition are, as in other EBUS regions, the dominant source of bias on the shelf (e.g. Shulman et al. (2013) for the Californian shelf).

2. Evaluation of the model biogeochemical variables

2.1. Nitrate

Nitrate profiles from the World Ocean Atlas 2018 database (17 in FMA, 10 in JAS; (Garcia et al., 2019)) were collected in the SSUS. They were compared with co-located model climatological profiles (Figs. S5 and S6). During the upwelling season (FMA), surface nitrate tended to be overestimated by the model over most of the outer SSUS shelf (Fig. S5a). Modelled vertical profiles reproduced well the high observed subsurface nitrate (~20-25 $\mu mol L^{-1}$ below 40-50 m) and offshore nitracline depth (~20 m) near 14°45'N, whereas the observed profiles collected offshore of the southern shelf (~12°30'N) displayed a deeper nitracline (~30 m depth) than in the model (Fig. S6a). Expectedly, observed and modelled nitrate surface concentration were much lower (~1-2 $\mu mol L^{-1}$) outside the cold season (i.e. in JAS; Fig. S5b). Modelled surface values were close but remained slightly higher than the observed. Subsurface observed values displayed a highly variable nitracline depth (20-50 m) whereas modelled nitracline depth was too shallow (~20 m; Fig. S6b).

Cross-shore sections (14°N) from the WOA 2023 1° resolution gridded climatology and from the model were also compared (Fig. S7). Overall model and data were in relatively good agreement. In contrast to the observed profiles shown in Fig. S6, modelled subsurface values (80-180 m depth) were higher (by ~3-5 $\mu mol L^{-1}$) than the observed during both the winter and summer seasons. Moreover, the relatively low nitrate values near the slope found in WOA 2023 may result from denitrification due to low oxygen concentration Machu et al. (2019), not reproduced by the model due to slightly too high subsurface DO (Figs. S2b,e).

2.2. Surface Chlorophyll-a

Due to the lack of in situ data, two satellite products are used to evaluate the model surface Chlorophyll (Chl-a). The spatial structure of the annual-mean surface Chl-a was well represented by the model with a maximum of ~3-4 $mgChlm^{-3}$ along the coast and lower values offshore (~0.5 $mgChlm^{-3}$ along 18°W; Figs. S8a-c). Chl-a concentrations were around 2-3 $mgChlm^{-3}$ between the 30 and 100 m isobaths for both the model and the observations. In the innershelf band (h<20 m), compared to SOM-NVA, the model tended to underestimate Chl-a (~2 $mgChlm^{-3}$) in the SSUS while fairly comparable values were found north of 15°N (~5 $mgChlm^{-3}$). The Chl-a cross-shore gradient over the inner shelf (along the 20-30 m isobath) was also stronger in SOM-NVA than in the model.

Seasonal variability of surface Chl-a concentration over the shelf was also relatively well reproduced by the model (Fig. S8d). During FMA, the model simulated a maximum Chl-a concentration around ~3 $mgChlm^{-3}$, slightly less than SOM-NVA. During JAS, lower Chl-a values (~1 $mgChlm^{-3}$) were found in model than in SOM-NVA (~2 $mgChlm^{-3}$). Uncertainties and biases associated with satellite measurements can be large, particularly in coastal environments (Chen et al., 2013). To illustrate this caveat we show the ESA-CCI climatological fields in Fig. S8d. Differences with SOM-NVA are substantial, especially in FMA. Although we are inclined to place more trust in SOM-NVA the discrepancies between the two products suggest that this model evaluation should be taken with caution.

Table 1: Shelf-averaged DO anomalies computed from the daily-averaged DO concentrations (ΔDO_a, in $\mu molkg^{-1}$) and from the double-time integrals of DO budget terms (ΔDO_b; see section 2.5). ϵ' is the relative error between the two terms ($\epsilon' = 100 \times \frac{|\Delta DO_a - \Delta DO_b|}{|\Delta DO_a|}$). FMA DO anomalies were averaged over the southern outer shelf(12°30'N-13°30'N, $30m < h < 50m$) while JAS DO anomalies were averaged over the central outer shelf(13°N-13°54'N, $30m < h < 50m$).

Seasons	FMA2015	FMA2016	FMA2017	FMA2018	FMA2019
ΔDO_a ($\mu molkg^{-1}$)	5.5	3.0	-21.6	-8.4	21.5
ΔDO_b ($\mu molkg^{-1}$)	10.6	1.6	-16.3	-24.2	28.2
ϵ'(%)	93	47	25	190	31

Seasons	JAS2015	JAS2016	JAS2017	JAS2018	JAS2019
ΔDO_a ($\mu molkg^{-1}$)	29.6	-49.3	33.9	-9.2	-5.0
ΔDO_b ($\mu molkg^{-1}$)	29.4	-47.9	37.1	-20.1	1.4
ϵ'(%)	0.7	2.9	9.4	120	130

References

Chabert, P., Capet, X., Echevin, V., Lazar, A., Hourdin, C., Ndoye, S., 2023. Impact of synoptic wind intensification and relaxation on the dynamics and heat budget of the south senegalese upwelling sector. Journal of Physical Oceanography 53, 1041–1067.

Chen, J., Zhang, M., Cui, T., Wen, Z., 2013. A review of some important technical problems in respect of satellite remote sensing of chlorophyll-a concentration in coastal waters. IEEE Journal of Selected Topics in Applied Earth Observations and Remote Sensing 6, 2275–2289. doi:10.1109/JSTARS.2013.2242845.

Echevin, V., Hauschildt, J., Colas, F., Thomsen, S., Aumont, O., 2021. Impact of chlorophyll shading on the peruvian upwelling system. Geophysical Research Letters 48, e2021GL094429.

Garcia, H., Weathers, K., Paver, C., Smolyar, I., Boyer, T.P., Locarnini, M., Zweng, M., Mishonov, A., Baranova, O., Seidov, D., J.R., R., 2019. World ocean atlas 2018, volume 3: Dissolved oxygen, apparent oxygen utilization, and dissolved oxygen saturation. NOAA Atlas NESDIS 83 3, 38. doi:https://archimer.ifremer.fr/doc/00651/76337/.

Machu, É., Capet, X., Estrade, P., Ndoye, S., Brajard, J., Baurand, F., Auger, P.A., Lazar, A., Brehmer, P., 2019. First evidence of anoxia and nitrogen loss in the southern canary upwelling system. Geophysical Research Letters 46, 2619–2627.

McCabe, R.M., Hickey, B.M., Dever, E.P., MacCready, P., 2015. Seasonal cross-shelf flow structure, upwelling relaxation, and the alongshelf pressure gradient in the northern california current system. Journal of Physical Oceanography 45, 209 – 227. doi:https://doi.org/10.1175/JPO-D-14-0025.1.

Montégut, C., Madec, G., Fischer, A.S., Lazar, A., Iudicone, D., 2004. Mixed layer depth over the global ocean: An examination of profile data and a profile-based climatology. Journal of Geophysical Research: Oceans 109.

Ndoye, S., 2016. Fonctionnement dynamique du centre d'upwelling sud-sénégalais: approche par la modélisation réaliste et l'analyse d'observations satellite de température de surface de la mer. Ph.D. thesis. Université Pierre et Marie Curie-Paris VI; Université Cheikh Anta Diop (Dakar).

Ndoye, S., Capet, X., Estrade, P., Sow, B., Dagorne, D., Lazar, A., Gaye, A., Brehmer, P., 2014. Sst patterns and dynamics of the southern senegal-gambia upwelling center. Journal of Geophysical Research: Oceans 119, 8315–8335.

Ndoye, S., Capet, X., Estrade, P., Sow, B., Machu, E., Brochier, T., Döring, J., Brehmer, P., 2017. Dynamics of a "low-enrichment high-retention" upwelling center over the southern senegal shelf. Geophysical Research Letters 44, 5034–5043.

Shchepetkin, A.F., McWilliams, J.C., 2003. A method for computing horizontal pressure-gradient force in an oceanic model with a nonaligned vertical coordinate. Journal of Geophysical Research: Oceans 108. doi:https://doi.org/10.1029/2001JC001047.

Shulman, I., Ramp, S.R., Anderson, S., Metzger, E.J., Sakalaukus, P., 2013. Impact of remote forcing, model resolution and bathymetry on predictions of currents on the shelf. Dynamics of Atmospheres and Oceans 61-62, 35–45. doi:https://doi.org/10.1016/j.dynatmoce.2013.03.001.

Tall, A., Machu, E., Echevin, V., Capet, X., Pietri, A., Corréa, K., Sall, S., Lazar, A., 2021. Variability of dissolved oxygen in the bottom layer of the southern senegalese shelf. Journal of Geophysical Research: Oceans , e2020JC016854.

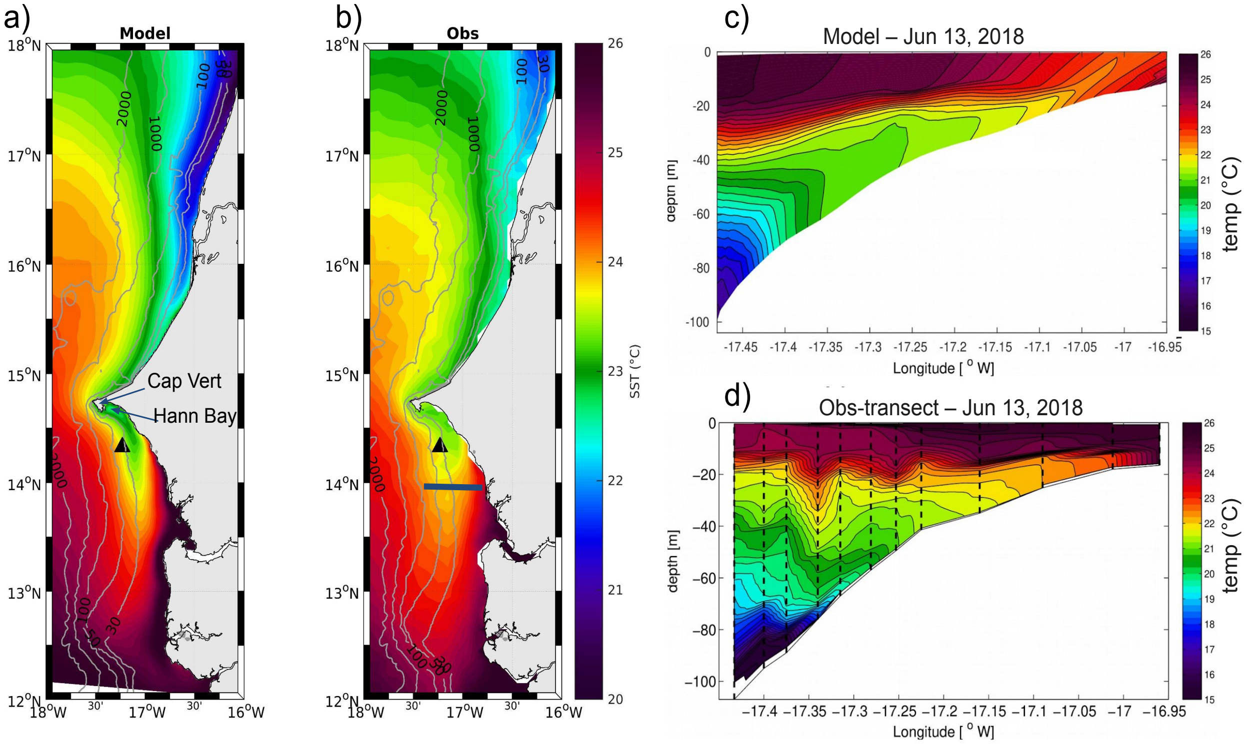

Fig. S 1: Sea surface temperature (SST) distribution from the (a) model and (b) CERSAT product averaged over 2016-2019. Zonal section of temperature at 14°N from the (c) model and (d) transect made on June 13^{th}, 2018. The triangle in (a) and (b) shows the Melax location and the line in (b) the location of the section.

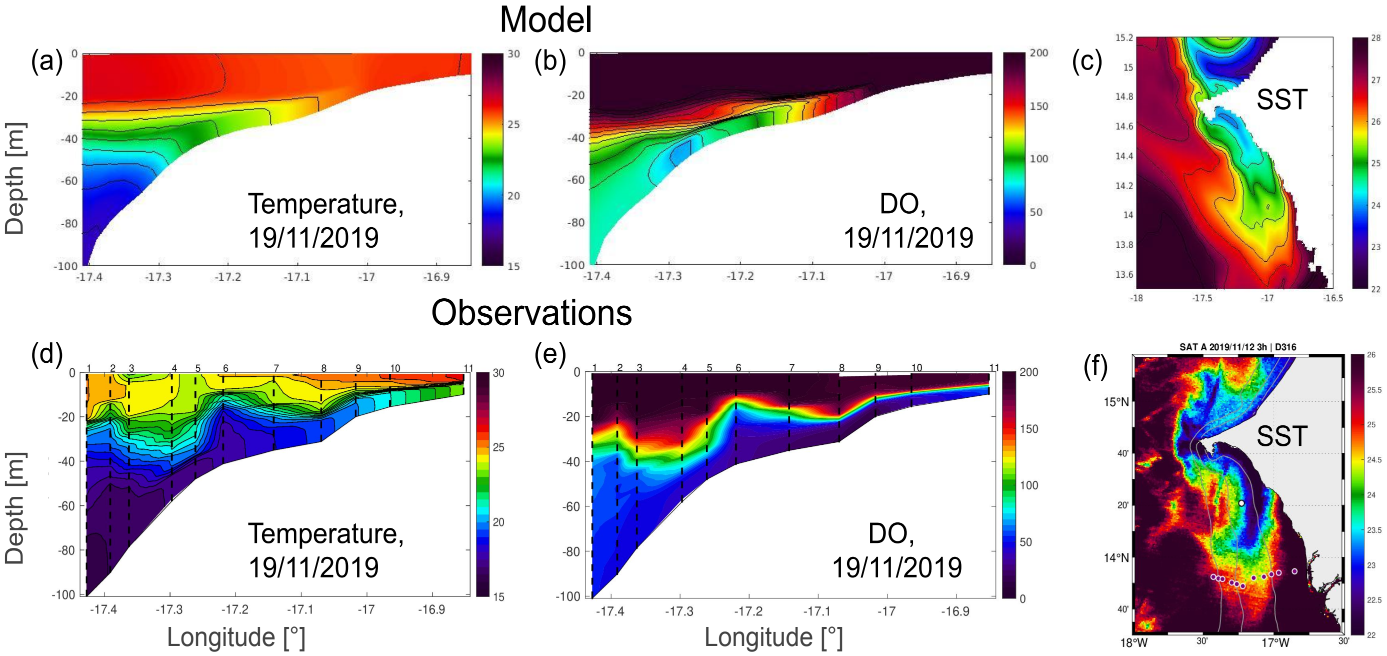

Fig. S 2: Zonal section (13°50'N) of (a,b) modelled and (d,e) observed temperature and DO on November 19^{th}, 2019. Modelled (c) and satellite (f) SST illustrating the upwelling event are also displayed.

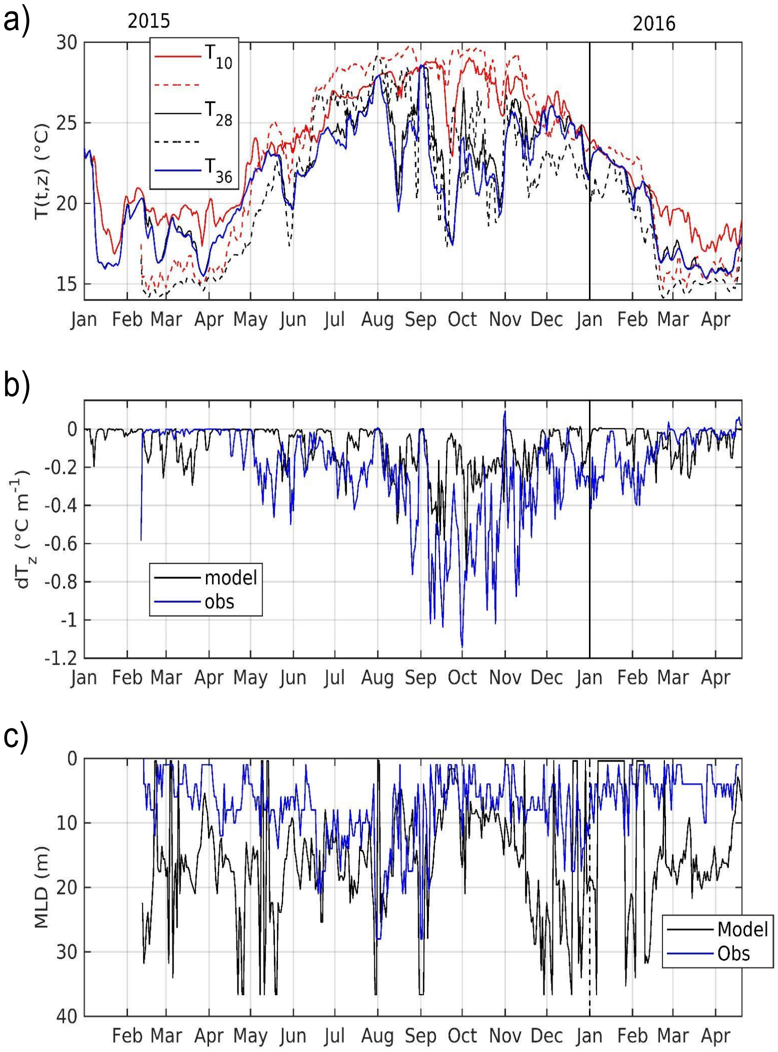

Fig. S 3: (a) Near-surface (10 *m*, red) and near-bottom (28 *m*, black) temperature time series from the model (solid lines) compared to observations (dashed lines) collected at the same depths at the Melax station. The time series of the bottom temperature (36 *m*, blue) of the model is also shown. (b) Time series of the temperature gradient between 25 and 28 *m* of the model (black) and Melax observations (blue). (c) Mixing Layer Depth (MLD) of the model (black) and Melax observations (blue) calculated as follows (T(z=1 *m*) - T(z = MLD) = 0.2°*C*; Montégut et al. (2004)). The period studied for the different figures is from January 2015 to the end of April 2016 at the Melax location, and the collected time series are smoothed to 1 day.

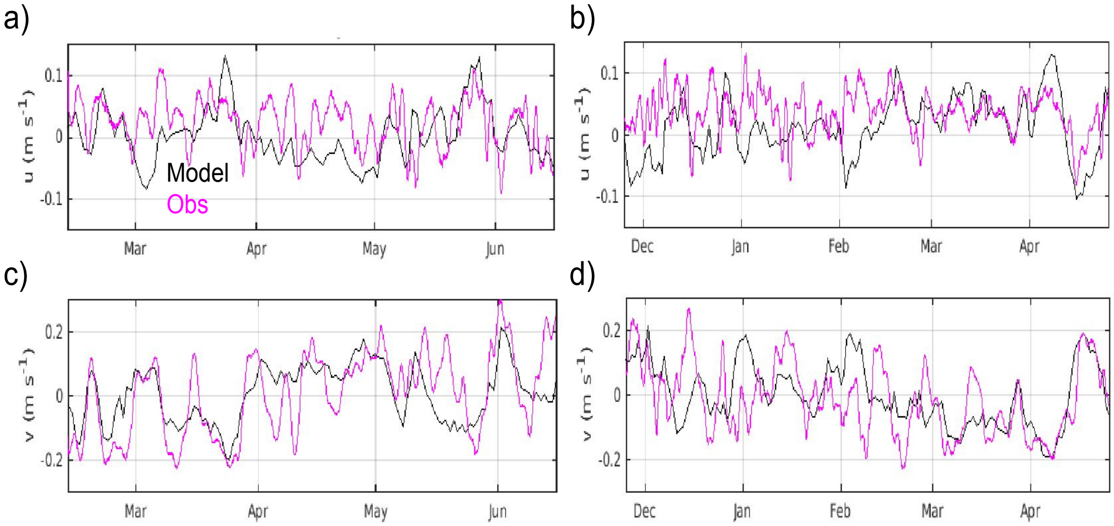

Fig. S 4: Depth-averaged (30-36 m) (a-b) zonal (u) and (c-d) meridional (v) current for model (black) and observations (magenta) from the Melax station during the periods of February 11^{th} to June 15^{th}, 2015 (left) and November 24^{th}, 2015 to April 26^{th}, 2016 (right). The model daily time series and 1-day smoothed observations are shown. Vertical ticks indicate the beginning of each month.

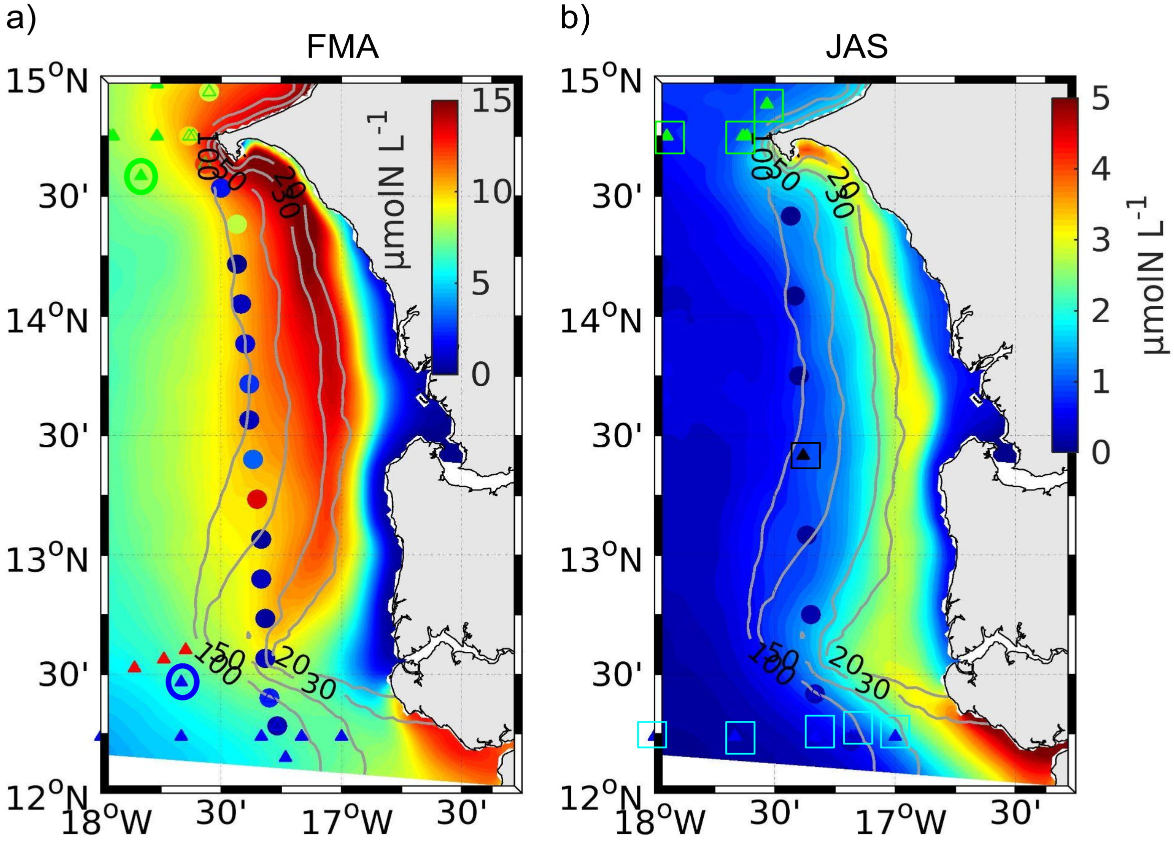

Fig. S 5: Model surface nitrate concentration in (a) February-April (FMA) and (b) July-September (JAS). Circles indicate observed surface values and triangles indicate the location of vertical profiles. The circles and triangles color indicate the surface nitrate values according to the color scales in (a) and (b). The triangles surrounded by a circle in (a) mark the position of the nitrate profiles where the maximum subsurface concentrations (~35 $\mu mol N L^{-1}$) are observed in Fig.6a. The squares in (b) highlight the position of the nitrate profiles in Fig. 6b.

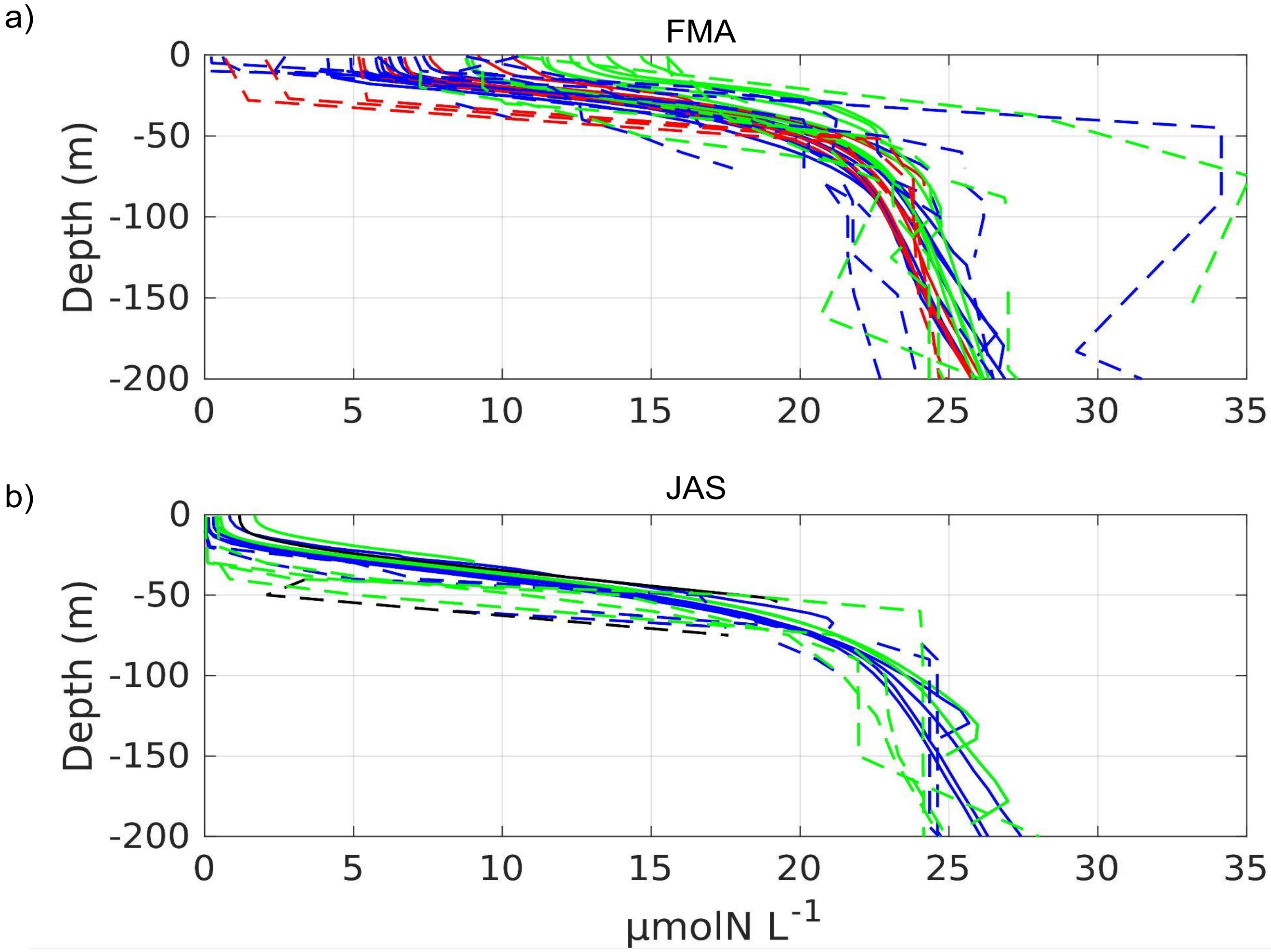

Fig. S 6: Nitrate vertical profiles in (a) FMA and (b) JAS. Dashed (full) lines indicate observations (model) values. Colors refer to the position of the profiles in figures S5a and S5b.

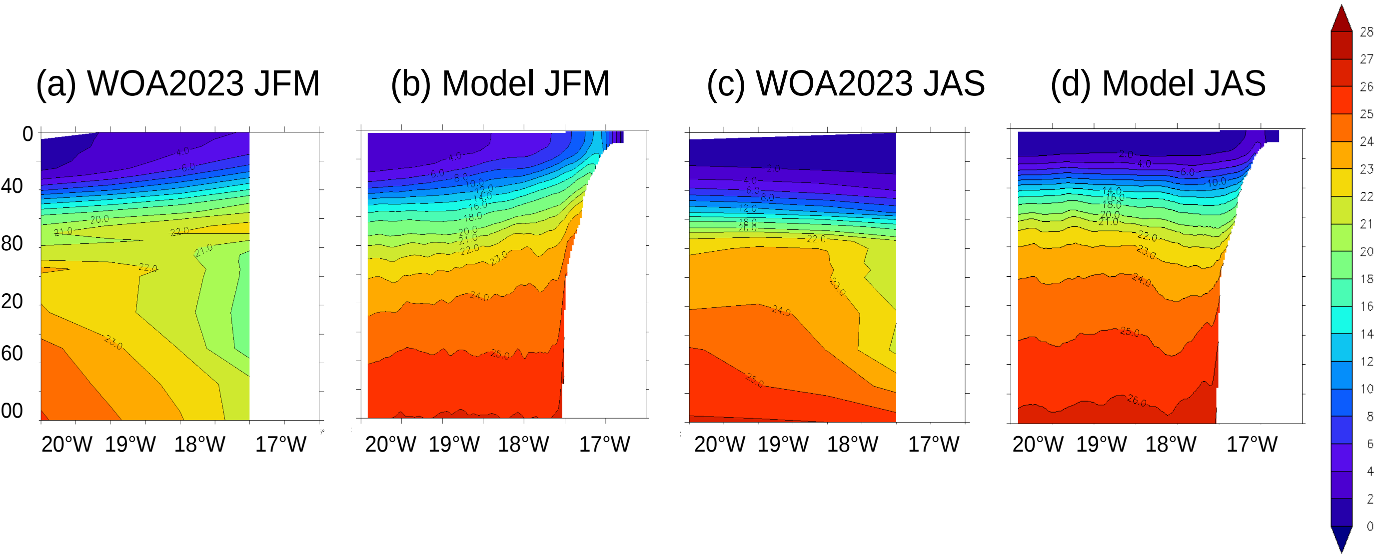

Fig. S 7: Zonal section (14°N) of observed (WOA2023) (a,c) and modelled (b,d) nitrate concentration (in $\mu mol kg^{-1}$) in winter (JFM) and summer (JAS) at 14°N. The model climatology is computed over the period 2015-2019.

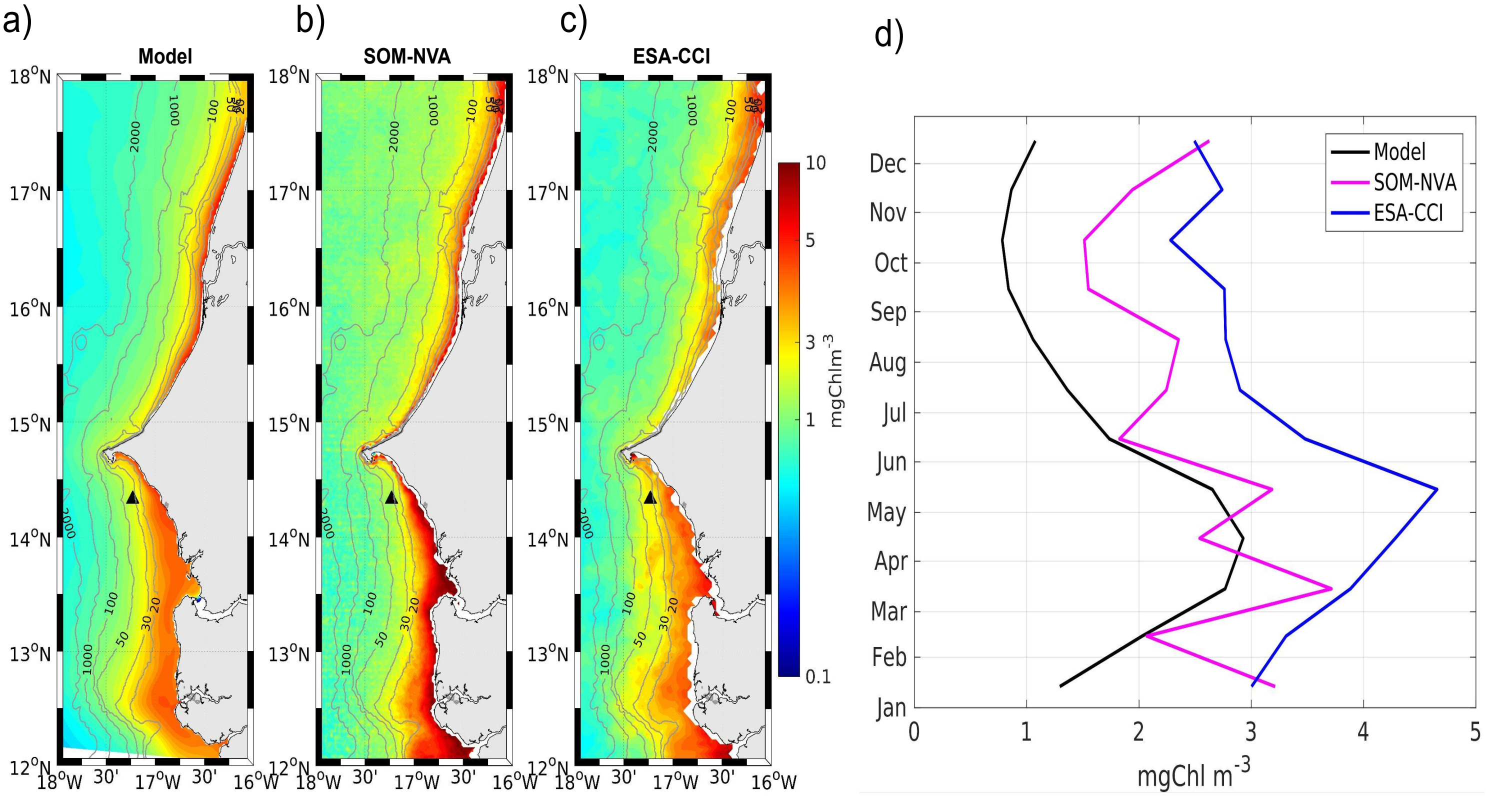

Fig. S 8: Annual mean surface chlorophyll-a (chl-a) concentration from the (a) model, (b) SOMNVA and (c) ESA-CCI products between 2015 and 2018. (d) Monthly average over the southern Senegalese shelf (12.5°N-14.6°N, 0-100 *m* isobaths) of the chl-a concentration of the model (black), SOM-NVA (magenta) and ESA-CCI (blue) products.

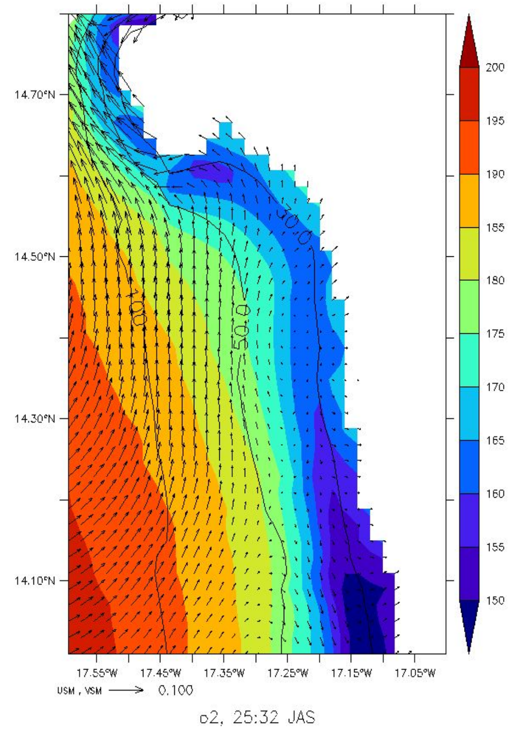

Fig. S 9: DO and horizontal velocity in JAS averaged over the 25-33 *m* depth range and from 2015-2019.

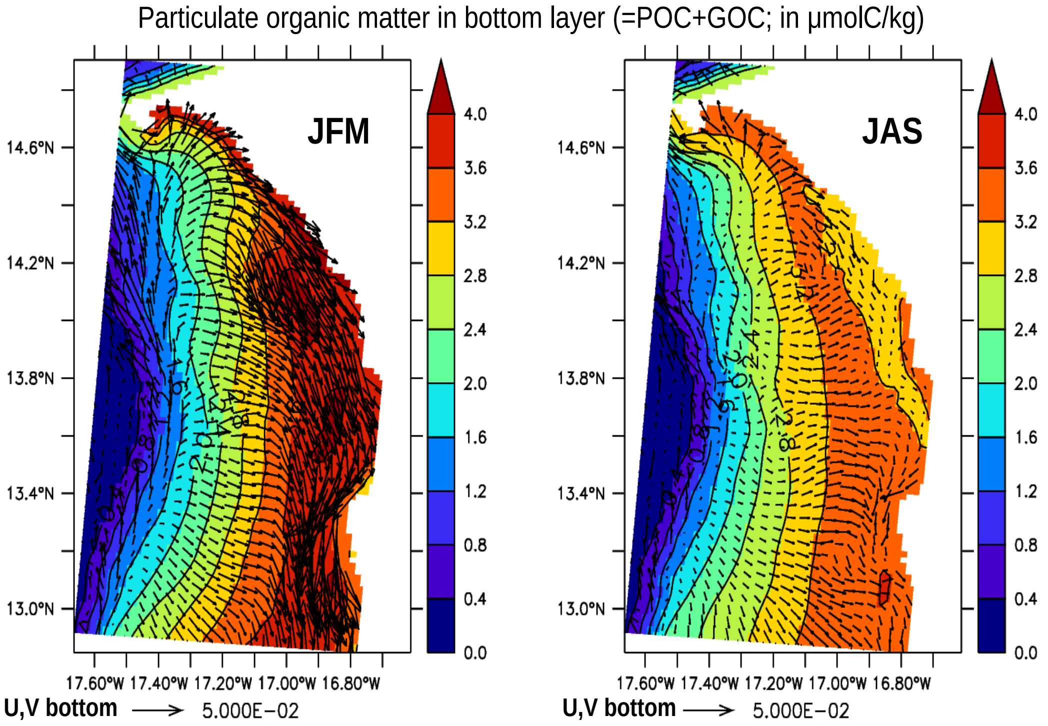

Fig. S 10: POM (POC+GOC; in $\mu molCkg^{-1}$) and horizontal velocity (in ms^{-1}) in the bottom layer, in JFM (left) and JAS (right) averaged from 2015-2019. Onshore currents nearly perpendicular to POM isolines indicate onshore transport of POM.

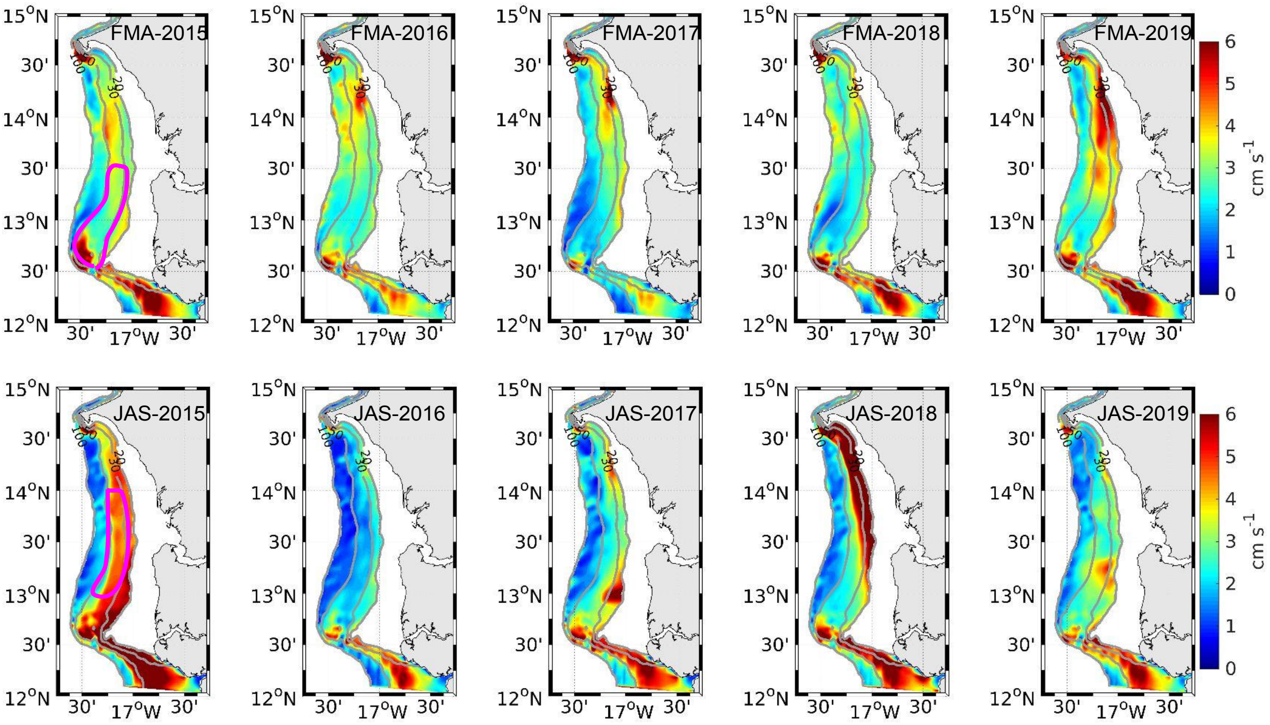

Fig. S 11: Maps of bottom velocity standard deviation. Standard deviation was computed with respect to the FMA or JAS temporal average. Note the lower standard deviation in FMA 2017 and JAS 2016 over the outer and mid-shelf. The magenta contours indicate the shelf portions over which U_{std} values were spatially averaged in FMA and JAS (see Table 1)

.

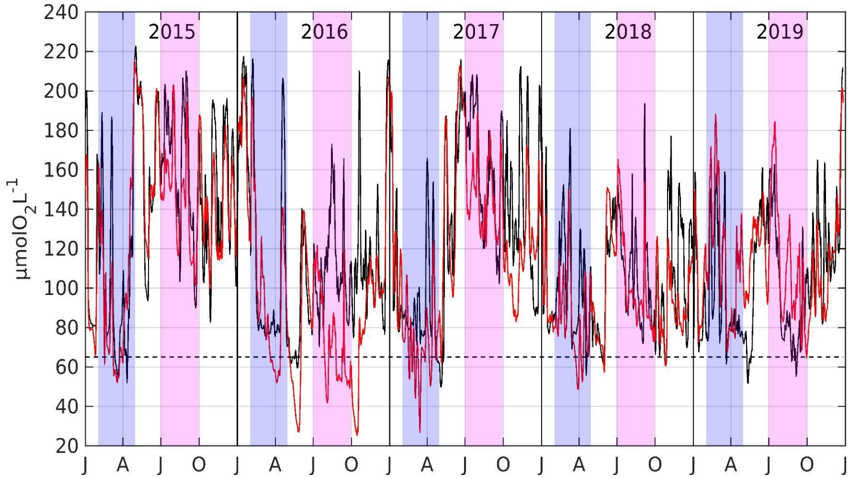

Fig. S 12: Time series (January 2015 to December 2019) of bottom DO, averaged between 30-50 *m* depth over the northern mid shelf (14.2°N-14.6°N, black) and over the southern mid shelf (12.8°N-13.5°N, red). The blue and pink color paths represent the cold season FMA and summer JAS respectively.

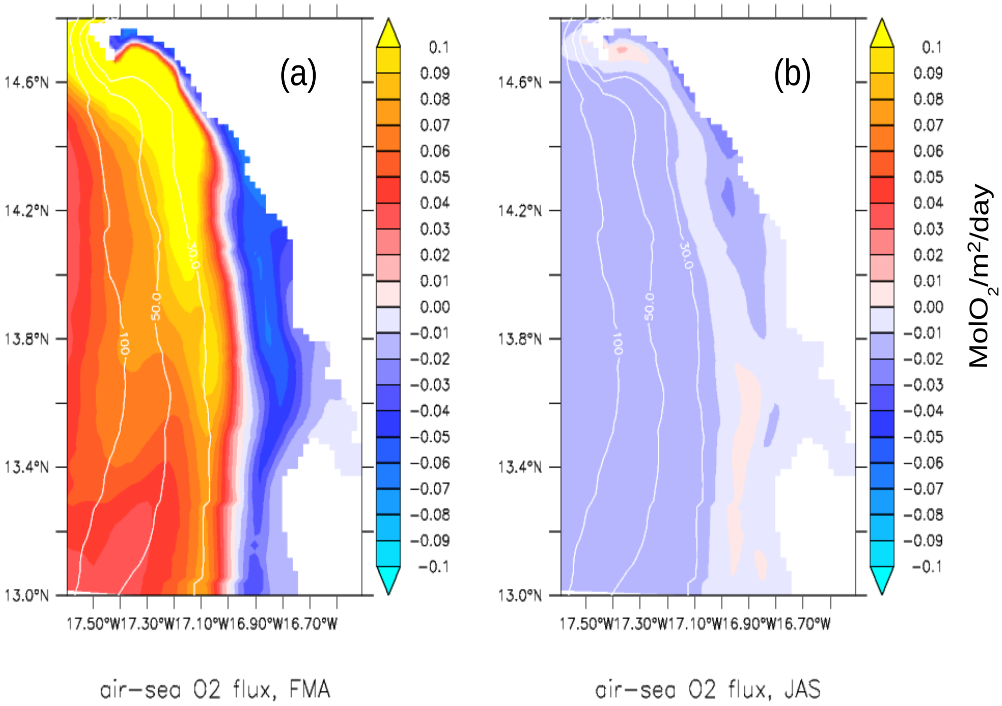

Fig. S 13: Air-sea oxygen flux (in molO_2 m^{-2}day^{-1}) in (a) FMA and (b) JAS averaged from 2015-2019. Note that a positive sign indicates oxygen flux into the ocean.